

Efficiency improvement of the solar chimneys by insertion of hanging metallic tubes in the collector: Experiment and computational fluid dynamics simulation

Loghman Rezaei^{c,1}, Samrand Saeidi^{a,b,*}, András Sági^a, M.R. Abdollahi Senoukesh^c, Gyula Gróf^d, Wei-Hsin Chen^{e,f,g}, Zoltán Kónya^a, Jiří Jaromír Klemes^h

^a Department of Applied and Environmental Chemistry, Interdisciplinary Excellence Centre, University of Szeged, Rerrich Béla Tér 1, Szeged 6720, Hungary

^b Biotechnology Center, Silesian University of Technology, 8 Krzywousty St., 44-100 Gliwice, Poland

^c School of Chemical, Petroleum and Gas Engineering, Iran University of Science and Technology (IUST), Narmak, Tehran, Iran

^d Center for Energy Research, Konkoly-Thege Miklós út 29-33, Budapest 1121, Hungary

^e Department of Aeronautics and Astronautics, National Cheng Kung University, Tainan 701, Taiwan

^f Research Center for Smart Sustainable Circular Economy, Tunghai University, Taichung 407, Taiwan

^g Department of Mechanical Engineering, National Chin-Yi University of Technology, Taichung 411, Taiwan

^h Sustainable Process Integration Laboratory (SPIL), NETME Centre, Faculty of Mechanical Engineering, Brno University of Technology - VUT Brno, Technická 2896/2, 616 00, Brno, Czech Republic

ARTICLE INFO

Handling Editor: Cecilia Maria Villas Bôas de Almeida

Keywords:

Solar chimney
Solar radiation
Collector efficiency
Hung metallic tubes
CFD simulation

ABSTRACT

The solar chimney power plant (SCPP) is a straightforward and clean technique to generate electricity from solar radiation. However, this technology still faces major challenges, such as low efficiency, which has hindered its industrialization. This study experimentally develops a novel collector design to improve the solar chimney collector's efficiency. The new design includes metallic tubes as solar radiation absorbers hung from the canopy of the collector. The metallic tubes are open at the top and sealed with transparent sheets at the bottom to decrease the solar radiation reflected into the ambient air. Experimental and 3-D computational fluid dynamics (CFD) analyses are performed to validate the new design. The effects of hanging metallic tubes on temperature and velocity distribution are explored. The temperature increased by about 5 K at the chimney inlet, causing a roughly 8% rise in collector efficiency due to the fact that metallic tubes operate as an extended surface. The impact of various tube geometries on solar chimneys' efficiency is examined. The CFD findings reveal that the metallic tube geometry variation has considerably impacted the collector's efficiency. Thus, the collector efficiency is increased by changing tube diameter by around 33.7%, similar to changing tube length by 30%.

1. Introduction

The solar chimney power plant (SCPP) is a straightforward and attractive clean technology to transform solar energy into electricity. While the technology is still in the experimental phase, it shows great potential as a way to reduce our reliance on fossil fuels and combat climate change (Kebabsa and Lounici, 2021). SCPP has simple components without complexities, including a collector as an essential element, a chimney, a turbine, and a power generator (Yapıcı et al., 2020). The collector is one of the main components for converting solar

radiation into thermal energy by heating the flowing air beneath the canopy. The canopy, which is the roof of the collector, has an appropriate distance from the ground. The chimney is located in the center of the collector, providing the proper conditions for the warmed-up air to flow radially inside the collector. The hot air flows naturally through the chimney due to its lower density than the cold ambient air outside the chimney (Al-Kayiem and Aja, 2016). The integrated turbine-generator unit is located in the chimney input section to receive the airflow kinetic energy and generate power (Mehranfar et al., 2022). As a semi-transparent medium, the canopy partly reflects and absorbs solar irradiation, but the major part is transmitted and absorbed by the

* Corresponding author. Department of Applied and Environmental Chemistry, Interdisciplinary Excellence Centre, University of Szeged, Rerrich Béla tér 1, Szeged 6720, Hungary.

E-mail address: samrand.saeidi@chem.u-szeged.hu (S. Saeidi).

¹ Author a,b and author c both contributed equally to this work.

<https://doi.org/10.1016/j.jclepro.2023.137692>

Received 6 January 2023; Received in revised form 22 March 2023; Accepted 2 June 2023

Available online 12 June 2023

0959-6526/© 2023 The Authors. Published by Elsevier Ltd. This is an open access article under the CC BY-NC-ND license (<http://creativecommons.org/licenses/by-nc-nd/4.0/>).

Nomenclature*Variables*

A_{coll}	Collector area (m ²)
A_{chim}	Chimney area (m ²)
d_{chim}	Chimney diameter (m)
D_t	Tube diameter (m)
C_p	Specific heat capacity of the air (J/kg K)
g	Gravitational acceleration (9.81 m/s ²)
H_{chim}	Chimney height (m)
H_{coll}	Collector height (m)
h	Heat transfer coefficient (W/m ² K)
h_f	Species enthalpy(energy/mass)
L	Characteristic length (m)
P	Air pressures in collector, chimney, and turbine (Pa)
R_i	Collector radial coordinate (m)
Ra	Rayleigh number
T_{ave}	Temperature average (K)
T_0	Air temperature in the inlet of the collector (K)
T_i	Air temperature in the inlet of the chimney (K)
\dot{m}	The mass flow rate of air through SCPP (kg/s)
G	Solar radiation (W/m ²)
V	Air velocity in the chimney (m/s)
ΔT	Temperature rise (K)
λ	Wavelength (mm)
η_{chim}	Chimney efficiency (%)
η_{ge}	Generator efficiency (%)
η_{coll}	Collector efficiency (%)
η_t	Turbine efficiency (%)
δ_s	Scattering coefficient
\varnothing	The phase function
Ω	Solid angle

Subscripts

Coll	Collector
Chim	Chimney

amb	Ambient
ave	Average
L_t	Vertical tube length
G_k	Turbulence kinetic energy generation due to the mean velocity gradients (j)
n	Refractive index
k	Turbulent kinetic energy (J/kg)
E	Energy (J)
S_h	Heat source in the energy equation
$I_{b\lambda}$	Black body intensity (W/m ²)
\vec{J}_i	Diffusion flux of species
\vec{v}	Overall velocity vector (m/s)
\vec{s}'	Scattering direction vector
x	Axial coordinate (m)
I	Radiation intensity (W/m ²)
J	Diffusion flux (kg/m ² s)

Greek symbol

α	Thermal diffusivity (m ² /s)
β	Coefficient of cubic expansion
ρ	Density of air (kg/m ³)
ε	Dissipation rate of turbulent kinetic energy (m ² .s ⁻³)
μ	Dynamic viscosity (Pa.s)
μ_t	Turbulent dynamic viscosity coefficient (Pa.s)

Abbreviations

CFD	Computational fluid dynamics
DO	Discrete ordinates
PVC	Polyvinyl chloride
SCPP	Solar chimney power plant
REI	Relative-Efficiency-Increase
No. I	Number
Exp	Experimental
Sim	Simulation

ground surface. The low power conversion efficiency of solar chimneys is a crucial technological problem for SCPP (Fallah and Valipour, 2022). It was revealed that the low-efficiency conversion of the SCPP was one of its fundamental problems when considering power generation. The efficiency of SCPP was improved mainly by increasing the collector diameter and chimney height, which is consistent with high-capacity electricity production demand. The low efficiency of SCPP originates from the collector's inefficiency, which is the main part and heart of this system (Koonsrisuk and Chitsomboon, 2013). However, there are a lot of technical and economic limitations to scaling up the SCPP (Guo et al., 2019). Moreover, it has been proven that SCPPs have low efficiency, but efficiency improves under hybrid and poly-generation modes. Other energy sources, such as geo-thermal energy, waste heat energy, and flared gas, can be utilized to increase the operation time of SCPPs (Sharon, 2023). Furthermore, combining SCPP with photovoltaic and geothermal energy has been proposed to increase daily power generation and improve performance in cloudy climates (Cao et al., 2014). Plus, a combination of a solar chimney and a cooling tower, called a "hybrid cooling-tower-solar-chimney (HCTSC)" has been proposed to increase the power output of a solar chimney up to 20 times under special conditions (Zou and He, 2015). Furthermore, Ozgen et al. (2009) experimentally analyzed the efficiency of a new double-flow solar air heater (SAH) using three different absorbing plates. The experimental set-up was constructed and tested in Turkey, and the efficiency of the SAH was determined from the experimental measurements. The study includes a comparison of the thermal efficiency of the SAH with

absorber plates made of aluminum cans against the efficiencies of other collectors with different absorber plate designs reported in the literature. Plus, Esen et al. (2009a) explored the use of artificial neural network (ANN) and wavelet neural network (WNN) models to predict the efficiency and air temperature leaving the collector unit of a SAH system with a double-flow aluminum cans absorber plate for three types of collectors. The study involves an experimental SAH system set up and tested in Turkey, and the data used for the modeling were obtained from measurements made in the SAH system. The study concludes that the proposed WNN model can be used to estimate the efficiency of SAHs with reasonable accuracy. The same research group (Esen et al., 2009b) discussed using a least-squares support vector machine (LS-SVM) to predict the efficiency of a SAH system with a double-flow aluminum cans absorber plate for three types of collectors. The study concludes that the proposed LS-SVM model can be used to estimate the efficiency of SAHs with reasonable accuracy.

In recent decades, several experimental setups of solar chimneys have been tested in different locations of the world (Saha et al., 2021). Investigations show that for the economical design of SCPPs with efficient power generation and high capacity, a large area of collector and a chimney with considerable height were required (Schlaich et al., 2004). Since the Manzanares operation results, there has been no interest in investing globally in the solar chimney power generation plant. Therefore, to overcome the economic limitations, some innovations have been proposed. According to theoretical investigations, a combination of the solar chimney with added heating channels has been presented, in

which heating channels can operate as heat exchangers (Al-Kayiem et al., 2012). Other proposals were based on the metallic plates' exploitation inside the collector chamber to intensify the absorption of solar radiation (Al-Kayiem et al., 2012). A solar chimney-coal-fired power generation combination system was proposed, in which the condenser released low-grade heat to preheat the air inlet to the solar chimney collector (Li et al., 2017). The effect of radiation transmission on power generation was investigated and compared with the transmission coefficients of Hedrick and Bernards (Pretorius, 2007). It was strongly suggested that insulating the collector's canopy at night prevents night-time waste of accumulated energy. Based on investigations, the main problems of SCPPs are: 1) low energy conversion efficiency; 2) wasting the high value of the received energy; and 3) oscillations in generated power during the day, month, and year (Pretorius, 2007).

Related to the design of the SCPP, the most influential parameters in the performance of solar chimneys are the chimney's height and the diameter of the collector area, representing the size of the plant. It can be

attributed to the increasing size of SCPP; the energy conversion efficiency would naturally increase (Dai et al., 2003). Al-Dabbas tested a typical solar chimney with 4 m of chimney height and 36 m² of collector area in Jordan. According to this experiment outline, the power generation capacity depended on solar radiation, input temperature to the chimney, and ambient temperature (Al-Dabbas, 2012). Furthermore, an experimental setup of SCPP at Zanjan University in Iran was tested, with a 12 m height of the chimney and a 10 m collector diameter. They focused on observing the air inversion phenomenon at the base of chimney. The air inversion occurred after sunrise and broke after warming up the collector (Kasaeian et al., 2011). Moreover, Ghalamchi et al. (2015) tested another SCPP in Iran at Tehran University with 1.5 m, 2 m, and 0.1 m of collector diameter, chimney height, and chimney diameter, respectively. They concluded from their experimental work that a smaller air input entrance gap for experimental work with a chimney height of less than 4 m improved the performance of the SCPP system. Furthermore, the SCPP in combination with the concentrated

Table 1

Summary of the studies relating to CFD simulation of SCPP.

Examined parameters	Collector diameter (m)	Chimney height (m)	Chimney diameter (m)	Highlights	Ref.
The effect of the second roof height on the system performance.	3.7	2.95	0.16	A new design was proposed, analyzed, and simulated, which used a secondary roof layer to improve the collector energy recovery efficiency. This technique was investigated both in parallel and in contour airflow inside the collector.	Nasraoui et al. (2020)
Impact of solar radiation on the airflow and the effect of turbine pressure drop on the power output of the SCPP.	244	195	10	Numerical simulations of SCPP adopting the fan model were presented. A mathematical model was set for the collector, chimney, and turbine regions to describe fluid flow and heat transfer. The standard k-ε model was applied as the turbulence model.	Rabehi et al. (2018)
The influence of collector inlet sizing on the optimization of solar chimneys.	2.75	3	0.32	The effect of collector roof height on the performance of the SCPP was studied from both experimental and simulation perspectives.	Ayadi et al. (2018)
Thermal efficiency of the system.	244	196	10.16	CFD simulation and thermal analysis were investigated in the case of using the surplus heat available in nuclear energy cycles as a secondary energy source for a solar chimney.	Fathi et al. (2018)
The effect of ambient crosswind on the solar updraft power plant system.	2000	500	–	They presented a brief review of SCPPs, including a simulation of applying radial partition walls (RPWs) inside the collector. They concluded that RPWs act effectively in improving the performance of collectors.	Ming et al. (2017)
The diverging angle of a chimney and the chimney opening diameter.	8	10	0.25–0.3	A CFD study using ANSYS-CFX was performed to optimize the geometrical parameters of SCPP and improve the flow characteristics.	Patel et al. (2014)
The influence of solar radiation and turbine pressure drop on the system's performance.	244	195	10	The greenhouse effect under the collector was simulated using the renormalization group theory (RNG) k-ε model for CFD simulation and implementing the discrete ordinate (DO) radiation model considered to solve the radiative transfer equation.	Gholamalizadeh and Kim (2014)
The impact of solar insolation, turbine pressure drop, and ambient temperature on SCPP performance.	244	194.6	10.16	A 3D numerical approach incorporating the radiation, solar load, and turbine models was verified by experimental data from a small plant in Manzanar, Spain, to show that the solar radiation model was important to be included in the simulation.	Guo et al. (2014)
Verifying a large range of chimney height (1 m–1000 m) by analytical scaling laws.	244	194.6	10.16	An unsteady CFD simulation using ANSYS Fluent was carried out to investigate a solar chimney model containing a chimney of 6 m in height.	Fasel et al. (2013)
The impact of different city locations in Iran on the SCPP performance.	244	200	10	A numerical model was developed to simulate the SCPP performance in different regions in Iran, and it was concluded that the southern areas of Iran were superior relative to the other regions.	Asnaghi and Ladjevardi (2012)
Effect of solar radiation, turbine pressure drop on the flow, heat transfer, and power output of the SCPP.	244	200	10	Numerical simulation of airflow, heat transfer and power output characteristics of an SCPP with an energy storage layer and the turbine was conducted similarly to the Spanish prototype. The amount of energy loss resulting from the exiting airflow from the chimney was investigated.	Xu et al. (2011)
Effect of solar radiation on the heat storage characteristics of the energy storage layer.	240	–	–	Different mathematical models were established for the collector, the chimney, and the energy storage layer of the solar chimney.	Ming et al. (2008)
The area ratio of the chimney outlet over the inlet, the divergent angle of the chimney wall, and the size of the system.	–	100–300	5–15	The effect of the geometry parameters of divergent chimneys on the performance of the SCPPs and the hydrodynamics of the system was investigated.	Hu et al. (2017)

solar power system was investigated. The maximum velocity in the regular operation was 2.2 m/s, which improved to a maximum of 2.72 m/s by using a secondary heat source (Sajjadi et al., 2021).

The simulation of the SCPP prototype was performed in Manzanares to compare the SCPP production capacity in two cities, Kuala Lumpur and Kerman. The results showed that the power plant efficiency was reduced by changing the stack configuration and angle from 27° to 45°. Kuala Lumpur was suitable for installing the SCPP (Arzpeyma et al., 2022). Based on results achieved via 3D simulation of SCPP, the steady-state current was an applicable assumption for solar radiation above 600 W/m². In addition, maximum air velocity occurred in a sloping SCPP at 800 W/m² radiation. Likewise, the maximum air velocity decreases as the chimney height is reduced (Fallah and Valipour, 2022). Another experimental study tested the effect of heat-absorbing materials in an SCPP with a 3 m collector diameter and a 3 m chimney height (Ghalamchi et al., 2016). Dimensional investigations revealed that the aluminum energy absorbent was better than the iron energy absorbent, and also, a 0.06 m input gap in the collector entrance gives the optimal performance of the equipment. Table 1 summarizes some references concerning the CFD simulations performed for SCPP.

The collector's performance has an essential impact on the efficiency of the SCPP. The higher collector's efficiency increases the solar radiation absorption and raises the air temperature, which causes an improved buoyancy force. Hence, in a conventional solar chimney, energy conversion efficiency depends mainly on the diameter of the collector and chimney height (Muhammed and Atrooshi, 2019). The transparent canopy of the collector transfers the solar radiation to the ground for convection with the airflow over it. Therefore, the heated soil transfers the heat to the flowing air over it. The canopy slope, height from the ground surface, and collector diameter are the essential parameters from a collector's energy generation viewpoint. The collector diameter effect on the generated energy is somehow more important than the effects of canopy height and slope (Cao et al., 2011). The problem of the collector geometry optimization for the better transference of energy is somehow complex since it depends on the solar radiation rate and the variations with day, month, and season.

The main objective of current research is to experimentally develop a new design of the solar chimney and then compare it with a CFD simulation. In this regard, a small-scale solar chimney is constructed by inserting metallic tubes that are hung from the canopy of the collector as a solar radiation absorber. In addition, the effect of hanging metallic tubes on air temperature and air velocity distributions has been investigated. Furthermore, the impact of hanging metallic tubes on the efficiency of the solar chimney is demonstrated in comparison to the no-tube case. Therefore, the CFD simulation carefully examines the effects of various metallic tube geometries on air temperature and air velocity distributions. Finally, the collector efficiencies of solar chimneys at various tube geometries are precisely studied and compared.

2. Experimental setup

The basic concept of the SCPP involves a chimney that is surrounded by a wide, sloping, transparent collector canopy. The canopy is angled so that it directs the sun's rays toward the base of the chimney. As the sun's rays hit the collector canopy, they heat up the air underneath. The scientific hypothesis behind the SCPP is that using solar radiation to heat

the air beneath the collector canopy creates a temperature difference between the air inside and outside the chimney chamber. This temperature difference causes the hot air to rise up the chimney, creating a buoyancy force. This buoyancy force can be harnessed to turn turbines and generate electricity.

In this research, we designed a new type of solar chimney with integrated metallic tubes, hung from the canopy of the collector to work directly as a medium for heat transfer to the airflow inside the collector. Indeed, optimal collector efficiency becomes more complex when hanging metallic tubes from the canopy of the collector compared with a conventional one. The complexity is because the mounting of metallic tubes inside the collector interferes with the heat transfer mechanism, which causes an increase in the number of effective parameters. However, it is inferred that hanging metallic tubes improves the collector's efficiency in converting the solar radiation into sensible heat for the air inside the collector chamber. The detailed mechanism of solar radiation heat transfer in the metal tube has been described in the appendix (Fig. S4).

In this setup, 120 metallic tubes 0.1 m in diameter are hung, which cover 10.4% of the area of the collector's canopy. The idea of hanging metallic tubes comes from the fact that the main origin of the low energy transmission efficiency in the solar chimney collector is based on the radiational reflections from the canopy to the outside, accompanied by convection heat losses to the ambient. The metallic tubes are hung from the canopy of the collector to reduce the solar radiation heat losses. The metallic tubes are open on top and closed at the bottom to let the radiation straightly enter the tube. Then, the metallic tube's wall is heated, and the heat is transferred to the flowing air inside the collector. The reflection of radiation by the canopy and the convection heat transfer between ambient air and the canopy surface are omitted in the sections covered by the metallic tubes. However, a small amount of convection heat loss from the open cavity effect of metallic tubes is expected. The high efficiency is a rough expectation since the only efficiency affecting the tube sections is the convection displacement of the hot air inside the tubes with the ambient air, which appears due to the open cavity effect. However, conductive heat transfer in the metallic tube sections might be negligible. The night-time power generation of a solar chimney with hung metallic tubes from the canopy of the collector is expected to be less than that of a conventional no-tube collector. Since the hung metallic tubes work as a shield to prevent solar radiation from reaching the ground, less heat is saved for night-time release. The collector is considered to be divided into eight sections. Each section includes 15 holes for the insertion of tubes to investigate the effect of metallic tubes on the performance of a solar chimney. Table 2 shows the physical properties of the materials used in constructing the tested solar chimney.

This solar chimney is tested in Tehran, where the solar radiation intensities are set at 800, 850, 930, 940, and 950 W/m² (Fadaei et al., 2018; Najafi et al., 2019). The maximum solar radiation was 950 W/m², and the maximum ambient temperature was 312 K. The city of Tehran has a geographical width and length of 35.7° and 51.4°, respectively (Sabziparvar and Shetaee, 2007). Table 3 includes the geometrical values of our solar chimney setup (Fig. S5).

The ground's surface is insulated to prevent heat diffusion into the deep layers of the ground. However, the heat stored in the collector chamber, wall, and canopy helps continue the night-time operation. The outside of the chimney is also insulated to prevent heat loss from the

Table 2
Physical properties of materials applied in the experimental solar chimney setup.

Physical property	Plexiglass	Air	Hung tube	Collector's ground (Soil)
Specific heat capacity (J/kg.K)	1466	1006.43	226	2016
Density (kg/m ³)	1170	Boussinesq approximation	7280	1700
Viscosity (kg/m.s)	–	1.789e-5	–	–
Thermal conductivity (W/m.K)	0.17–0.25	0.024	66.8	0.779

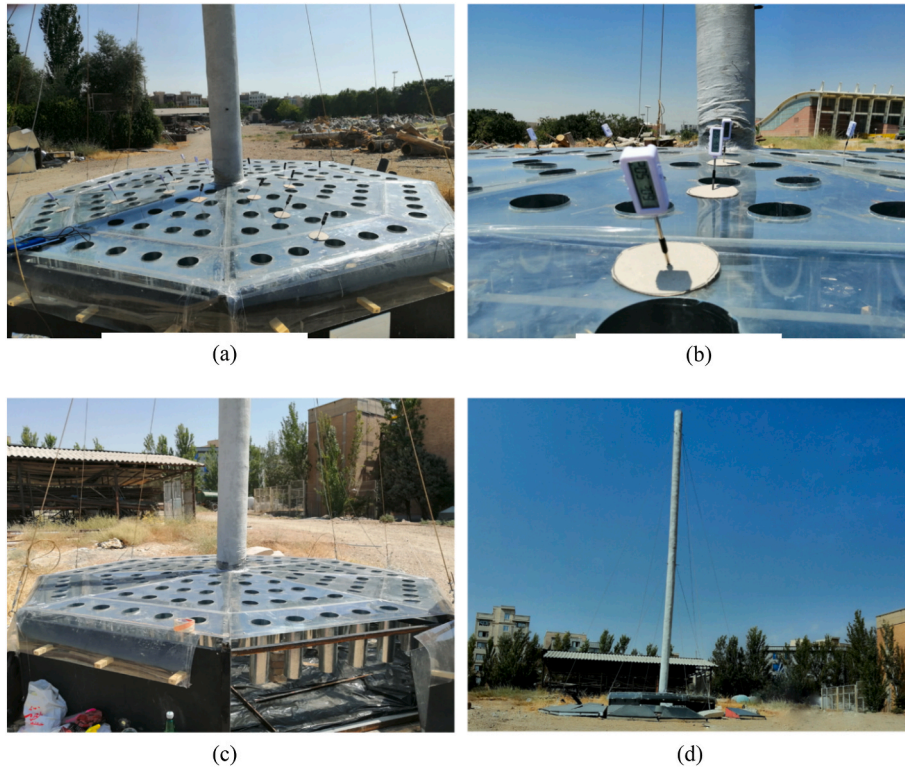


Fig. 2. Schematic of our experimental solar chimney setup, (a) collector and the tubes in an overall view including the thermometers, (b) digital thermometers and shields used for air temperature measurements inside the collector, (c) side-view of hung metallic tubes from the canopy of the collector, (d) overall view of the experimental solar chimney setup.

Momentum equation:

$$\nabla \cdot (\rho \vec{v} \vec{v}) = -\nabla p + \nabla \cdot \left(\mu \left[(\nabla \vec{v} + \nabla \vec{v}^T) - \frac{2}{3} \nabla \cdot \vec{v} \mathbf{I} \right] \right) + \rho \vec{g} \quad (3)$$

Energy equation:

$$\nabla \cdot (\vec{v} (\rho E + p)) = \nabla \cdot \left(k_{\text{eff}} \nabla T - h_f \vec{j} + \left(\mu \left[(\nabla \vec{v} + \nabla \vec{v}^T) - \frac{2}{3} \nabla \cdot \vec{v} \mathbf{I} \right] \cdot \vec{v} \right) \right) + S_h \quad (4)$$

where E , g , h_f , J , I , t , T , μ , \vec{v} , S_h , and k_{eff} are: energy, acceleration of gravity, specific enthalpy, diffusion flux, radiation intensity, time, temperature, dynamic viscosity, overall velocity vector, the heat source owing to incident solar radiation, and effective conductivity, respectively (Guo et al., 2015).

The Rayleigh number should be checked to see whether the flow is sufficiently turbulent or not to decide on selecting the appropriate model for simulating the system. The Rayleigh number is defined in Eq. (5) as follows:

$$Ra = \frac{g \beta \Delta T L^3}{\alpha \nu} \quad (5)$$

where ΔT , β , α , and L represent the maximum temperature difference, thermal expansion coefficient, thermal diffusivity, and height of the collector, respectively. In our case, the Rayleigh number is calculated higher than 10^{10} , which suggests using the turbulence model in simulation (Rabehi et al., 2018). The standard $k-\epsilon$ is used as the turbulence model in the numerical simulation; k is the turbulent kinetic energy and ϵ is the dissipation rate (Eq. (6) and (7)).

$$\frac{\partial}{\partial x_i} (\rho k u_i) = \frac{\partial}{\partial x_j} \left[\left(\mu + \frac{\mu_t}{\delta_k} \right) \frac{\partial k}{\partial x_j} \right] + G_k + G_b - \rho \epsilon - Y_M \quad (6)$$

Eq. (7) for the energy dissipation ϵ :

$$\frac{\partial}{\partial x_i} (\rho \epsilon u_i) = \frac{\partial}{\partial x_j} \left[\left(\mu + \frac{\mu_t}{\delta_\epsilon} \right) \frac{\partial \epsilon}{\partial x_j} \right] + C_{1\epsilon} \frac{\epsilon}{k} \left(G_k + G_b C_{3\epsilon} \right) - C_{2\epsilon} \rho \frac{\epsilon^2}{k} \quad (7)$$

In Eqs. (6) and (7), G_k is the generation of turbulence kinetic energy because of the mean velocity gradients, G_b represents the generation of turbulence kinetic energy as a result of buoyancy, Y_M is the energy production term due to the flow of flow compressibility. The $k-\epsilon$ turbulence model constants are defined by: $C_{1\epsilon} = 1.44$, $C_{2\epsilon} = 1.92$, $C_{3\epsilon} = 0.09$, $\mu_t = \frac{C_{\mu} \rho k^2}{\epsilon}$, $\delta_\epsilon = 1.3$, $\delta_k = 1, 0$.

3.2. Radiation model

The DO radiation model can solve the radiative transfer equation (RTE) for some of the discrete angles that are associated with vector directions fixed in the global Cartesian system (x ; y ; z). In the DO model, the RTE equation is solved in the direction of the \vec{s} and as well as a field equation. Therefore, it can be rewritten as Eq. (8). CFD software such as Ansys Fluent can simulate non-gray radiation using the gray-band model. In this context, the RTE equation is created to determine the spectral intensity of I_λ as equation Eq. (9) (ANSYS Inc, 2013).

$$\nabla \cdot (I(\vec{r}, \vec{s}) \vec{s}) + (a + \delta_s) I(\vec{r}, \vec{s}) = a n^2 \frac{\delta T^4}{\pi} + \frac{\delta_s}{4\pi} \int_0^{4\pi} I(\vec{r}, \vec{s}') \varnothing(\vec{r}, \vec{s}') d\Omega' \quad (8)$$

$$\nabla \cdot (I_\lambda(\vec{r}, \vec{s}) \vec{s}) + (a_\lambda + \delta_\lambda) I_\lambda(\vec{r}, \vec{s}) = a_\lambda I_{b\lambda} + \frac{\delta_\lambda}{4\pi} \int_0^{4\pi} I_\lambda(\vec{r}, \vec{s}') \varnothing(\vec{r}, \vec{s}') d\Omega' \quad (9)$$

At each wavelength interval, the RTE is integrated, which leads to transport equations for I_λ , $\Delta\lambda$, and the radiant energy existing in the wavelength band $\Delta\lambda$. Therefore, in each direction \vec{s} and position \vec{r} , \vec{s}' scattering direction vector, the value of total intensity $I(\vec{r}, \vec{s})$ is

calculated using Eq. (10) as follows:

$$I(\vec{r}, \vec{s}) = \sum_k I_{\lambda_k}(\vec{r}, \vec{s}) \Delta\lambda_k \quad (10)$$

where the summation is over the wavelength bands.

3.3. Solution procedure

The SIMPLE algorithm is applied to interlock the momentum, continuity, and pressure equations. There is a 10^{-5} limitation for the continuity term and a 10^{-6} for the remaining terms during convergence calculations. The following simplification assumptions are used in CFD simulation to improve the speed of calculations. The assumptions that are applied to solve the equations are: 1) steady 3D fluid flow and heat transfer inside the collector and chimney; 2) single-phase and compressible fluid flow; 3) consistent fluid and solid material thermodynamic properties; 4) heat loss is ignored where the chimney wall is insulated; 5) turbulent airflow is assumed, and the k- ϵ model and k- ϵ realizable models are used; 6) for near-wall treatment, standard wall function is used; 7) inside the computational domain, refined grids near the walls, 3D structured grids, and the standard wall functions with $30 < y^+ < 300$ have been chosen for simulating the near-wall treatment of the turbulent flow.

3.4. Boundary conditions

The surrounding temperature is 303–312 K; the ambient temperature is considered constant for each hourly interval during the simulation. Because the chimney wall and ground surface are insulated, the heat transfer at the collector's ground (A) and the heat transfer from the chimney wall (G) to the surrounding area are set to zero. The boundary conditions of the wall, which has convective heat transfer with the air inside the collector, are the collector wall (B) and the hung metallic tube (F). The transparent collector cover (D) and the bottom of the suspended tubes (E) are assumed to transmit 85% of the energy. The boundary conditions at the input to the collector (C) and the output from the chimney (H) are taken at a pressure outlet equal to atmospheric pressure. Because of the axial simplicity of the geometry, the 3D CFD calculations are done on one of the eight portions of the octagonal geometry of the collector to save calculation time and memory requirements on the computer. For this simplification assumption, one needs to assume that all the eight octagonal sections of the collector

equally receive sunlight radiation. A periodic boundary condition should be chosen as the required option to calculate the above conditions in the software. All the considered boundary conditions in the simulation are illustrated in Fig. 3.

A summary of the considered boundary conditions for the solar chimney simulation is given in Table 4.

3.5. Geometry and mesh independency

As shown in Fig. 4, the Gambit software is utilized to generate a mesh in geometry of solar chimney. Since the collector configuration looks like octagonal geometry, the sun is supposed to radiate constantly perpendicular to the canopy of the collector to reduce the calculation time by calculating one part of the eight parts of the collector. In this way, all eight individual compartments of the collector are supposed to receive the exact value of radiation, resulting in a considerable reduction in calculation time in each run. The CFD simulation code is executed using a Core i7-6800K-3.4GHz processor with 32 GB of installed RAM, operating on Windows 10.

Different mesh sizes are considered for maintaining grid independence, comparing the temperature and average velocity of the airflow inlet of the chimney to obtain an accurate solution (Krzywanski et al., 2020a). The finer mesh size can capture more detail and provide a more accurate representation of the airflow, resulting in more reliable results (Krzywanski et al., 2020b). In the present work, all simulations are performed with a fine mesh. Three-dimensional hexahedral cells (type: cooper), and the fine mesh sizes have been considered to range from 0.8 to 1.1 cm. However, to compare with other works and validate the mesh performance, four meshes are tested in the present work. An attempt is made to use as many meshes as possible in order to achieve the best possible result in the shortest time. Therefore, a mesh independence test is performed to find the optimal mesh. In this way, by performing several simulations with different meshes, the results of the respective simulations are compared, and the method that provided the least execution time and acceptable data in the simulation is selected as the optimal mesh. Then numerical findings are validated with experimental data to show the properness of CFD simulation performed in this study. Table 5 shows the number of meshes used in different calculations for no-tube and tube-added conditions. Two cases (no-tube and 120 tubes) are evaluated by comparing the number of cells. It is clear that temperature (T_{Chim} sensor), the best parameter, can be fixed at a high cell configuration.

4. Results and discussion

4.1. Experimental results

The experimental data are collected hourly from 10:00 to 19:00 for approximately one month in August 2019 at the IUST in Tehran. Since windy and cloudy weather or shadow conditions severely affect data accuracy, appropriate hours and days are chosen with minor wind and cloudiness conditions. The windy weather lets some excess cold air in from one side of the collector and prevents air from entering from the opposite side. Furthermore, reporting uncertainty calculations for

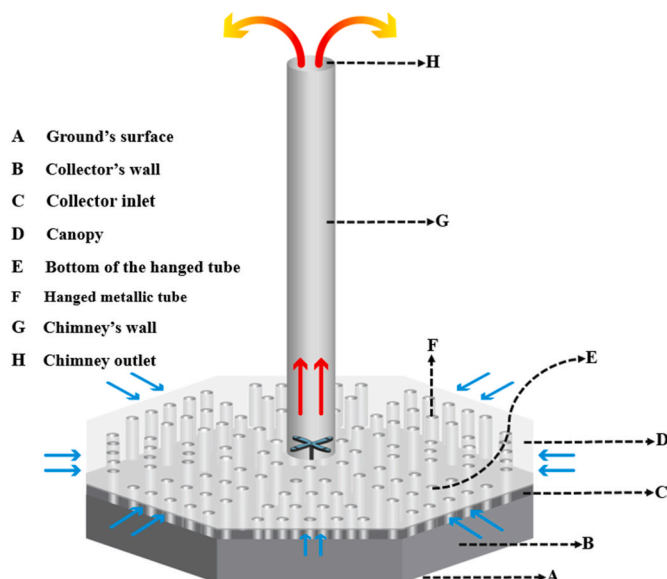


Fig. 3. Schematic of the solar chimney with considered boundary conditions.

Table 4
Boundary conditions for the solar chimney simulation.

Place	Type	Value
Chimney's wall	Adiabatic	$Q_{\text{chim}} = 0$
Canopy	Radiation transmission	$Q_{\text{Radiation}}$
Ground's surface	Adiabatic	$Q_{\text{Ground}} = 0$
Collector inlet	Pressure inlet	$P_i = 0 \text{ Pa}$, $T_0 = 312 \text{ K}$
Chimney outlet	Pressure outlet	$P_o = 0 \text{ Pa}$
Collector's wall	Heat transfer	$h = 8 \text{ W}/(\text{m}^2 \cdot \text{K})$
Hung metallic tube	Heat transfer	$h = 8 \text{ W}/(\text{m}^2 \cdot \text{K})$
Bottom of hung tube	Radiation transmission	$Q_{\text{Radiation}}$

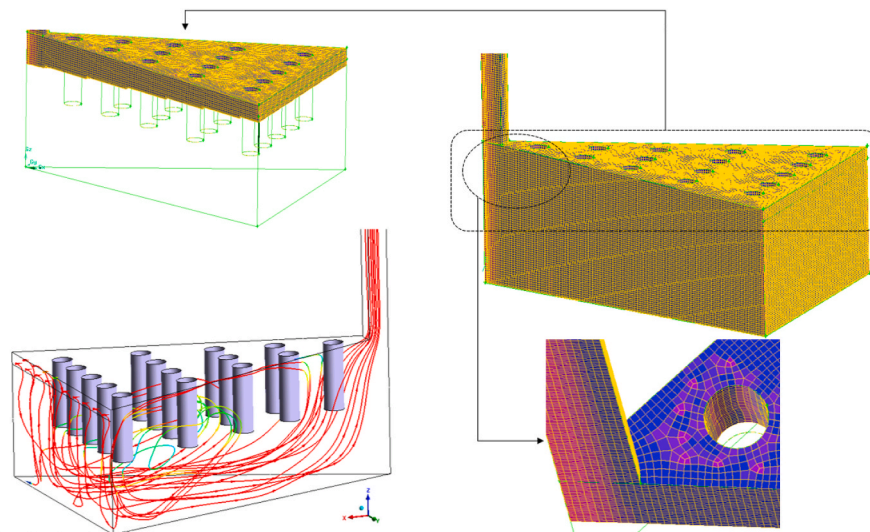


Fig. 4. 3D model and meshing of the collector in the GAMBIT.

Table 5
Meshing size configurations.

Case 1 (No-tube) No. cells	T (K)	Time	Case 2 (120 tubes) No. cells	T (K)	Time
300,000	322.3	12 h	500,000	327.7	17 h
530,000	326.2	17 h	700,000	329.3	2 days
710,000	327.4	2 days	1,000,000	329.5	3 days
960,000	327.5	2.5 days	1,300,000	329.6	5 days

outdoor pilot plants that function in relation to weather and solar radiation, such as solar chimney power plants, can be challenging due to the variability in climate and solar radiation. Because these factors can change rapidly and unpredictably, it can be difficult to repeat experiments or measurements precisely. Nevertheless, uncertainty calculation has been reported in Appendix section A.4.

Since our collector size is small, even in severe windy conditions, some hot air from the collector may exit on the opposite side into the surrounding area. Therefore, to decrease the extent of the temporary wind effect on the continual operation condition of the solar chimney, the upper side of the inlets of the canopy are bent down 0.15 m around the collector chamber, as illustrated in Fig. 1. However, the corrupted data from excessive wind gusts is discarded to be replaced with correct data from another day. Fig. 5 represents the variation of collector temperatures at three different radii, averaged from four measurements around the collector at various radii, for both hung metallic tubes and

no-tube conditions. Fig. 5 clearly shows the temperature increase from higher radii toward lower radii. The data has some deviations from the trend. The variations can be attributed to the slight wind blowing or trivial cloudy conditions. However, the trends in the graphs represent the real expectations for the effects of hanging metallic tubes.

When one compares the two sections of Fig. 5 at the extremum points at 13:00, reveals around a 4 K temperature increase resulting from hanging 120 metallic tubes from the canopy of the collector. From Fig. 5, it can be concluded that, first, the higher temperature is achieved by a collector with 120 tubes in comparison to the no-tube case. Second, the digital thermometers indicate that temperature differences in the noon hours (12:00 onwards) are slightly different in the 120 metallic tube case compared to the no-tube case, meaning that all digital thermometers approximately show the constant temperature in the no-tube case. In other words, the collector with added tubes performs better in terms of energy loss. It also concludes that the radiation heat absorption by metallic tubes is high during the morning hours, and it helps to make the temperature rise at different solar radiation levels from 12:00 onward in the 120-tube case. Due to the lack of space in the legend, “120 hung metallic tubes” were replaced with “120 tubes”.

Fig. 6 represents the temperature variations versus time in the entering airflow into the collector (T_0) and the entrance of the chimney (T_i) for the two cases (no-tube and 120 tubes) that operated on two successive days. The graph shows that the ambient temperature in the case of the hanging metallic tubes is lower than on the day of the no-tube condition. However, the measured temperature at the chimney zone is

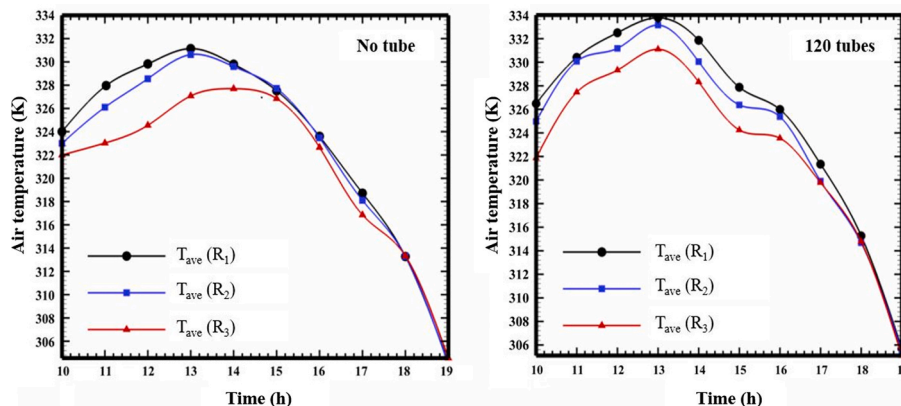


Fig. 5. Average air temperature variation versus time for both cases: no-tube and 120 metallic tubes. Ri: Radial coordinate of the collector (m).

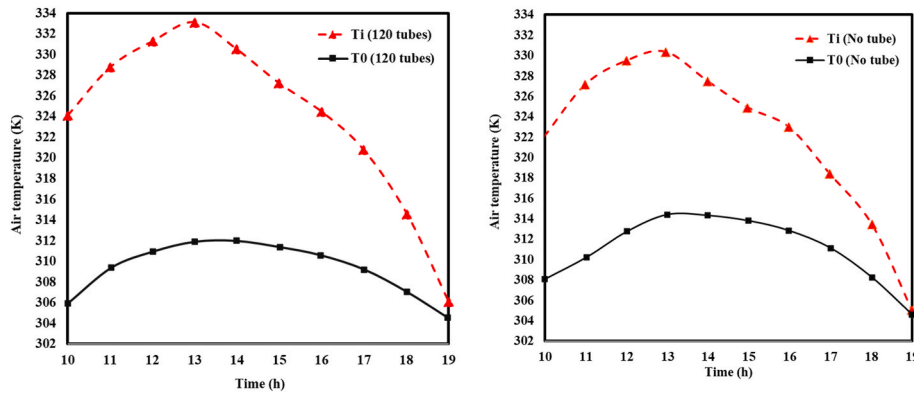


Fig. 6. Air temperature variations versus time in the entrances of the collector and chimney measured for two successive days in both cases of no-tube and 120 tubes.

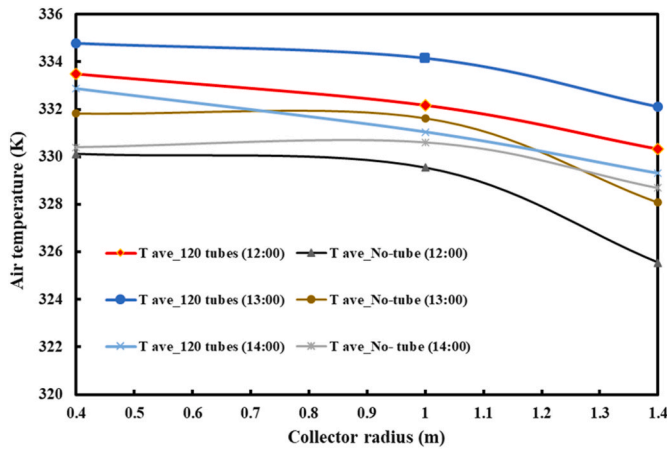


Fig. 7. Average air temperature versus collector radius for different time-hours and both cases (no-tube and 120 tubes).

higher than that of the no-tube condition. Fig. 6 shows around a 22 K increase for the case of 120 tubes compared to 16.5 K for the no-tube case given at 13:00.

Fig. 7 depicts the average air temperature variations versus collector radius at various measuring times within the collector from 12:00 to 14:00 for both the no-tube and 120-tube cases. The maximum air temperature in the 120-tube case occurs at 13:00. The minimum is in the no-tube case at 12:00. Moreover, it can be seen that a uniform (linear) decrease with the increase of the radius of the collector happens for all trends of 120-tube case. In contrast, the trends for no-tube cases are not linear because of air circulation inside the collector.

Hanging the metal tubes from the canopy absorbs solar radiation more effectively and improves the heat transfer of solar radiation into the airflow inside the collector. Therefore, it also causes increased air velocity inside the collector and chimney. Fig. 8 depicts the variation of measured air velocity versus time for no-tube and hung metallic tubes at 0.6 m from the chimney structure. The trend of measured air velocity versus time variations is comparable with Figs. 5 and 6, showing an increase and a decrease during morning and afternoon times, respectively.

The overall efficiency of the SCCP is the product of the individual efficiencies of the system (Nizetic et al., 2008), as Eq. (11) shows.

$$\eta_{sccp} = \eta_{chim} \eta_{coll} \eta_t \eta_{ge} \quad \text{Eq. (11)}$$

Usually, for the experimental set-ups of the solar power plant, the turbine and generator are not installed due to the high cost and a possible error in the speed measurement. In our work, the experimental system was without a generator and turbine. According to Eq. (11), a

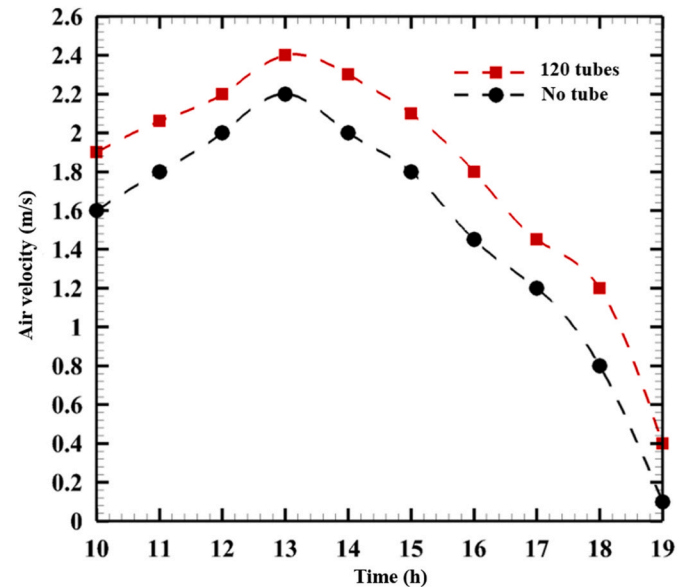


Fig. 8. The variations of measured air velocity versus time inside the chimney for both cases of no-tube and 120 tubes.

constant number for the efficiency of the turbine and generator can be assumed to be 0.8 and 0.95, respectively. Thus, the overall efficiency depends on the collector and chimney efficiencies, so by increasing the collector's efficiency, the overall efficiency increases. The efficiency of the collector is given in Eqs. (12) and (13) as follows (Nizetic et al., 2008; Zhou and Xu, 2016):

$$\dot{m} = \rho V A_{chim} \quad (12)$$

With replacing \dot{m} (kg/s) in Eq. (12), the following result is obtained:

$$\eta_{coll} = \frac{\text{Thermal power}}{\text{Radiation energy}} = \frac{\dot{m} c_p \Delta T}{G A_{coll}} = \frac{\rho V A_{chim} c_p \Delta T}{G A_{coll}} \quad (13)$$

Using the input and output measured temperatures of the collector shown in Fig. 1, Eq. (13) can be used to calculate the collector's efficiency for both no-tube and hung metallic tube cases. At the maximum solar radiation at 13:00, the efficiency stood at 25% and 33.9% for the no-tube and the added metallic tube cases, respectively. A 35.6% increase in overall efficiency is achieved by using 120 pieces of tubes with a 0.1 m diameter and 0.33 m height and a 0.5 mm wall thickness in the collector with a 9.7 m² land area, occupying 10.4% of the total collector's area.

The data in Table 6 summarizes the collector efficiency during various day-times. The relative efficiency increase (REI) indicates the

Table 6
Collector efficiency at different times of experiments for all cases.

Case	Time (h)				
	11:00	12:00	13:00	14:00	15:00
120 tubes	29.7%	30.1%	33.9%	28.5%	25.2%
No-tube	22.7%	24.7%	25%	22.4%	19.2%
Relative-Efficiency-Increase (REI)	30.8%	17%	35.6%	27.2%	31.2%

efficiency of the 120-tube case compared to the no-tube case, where the maximum efficiency is gained at 13:00 (35.6%). Furthermore, it varies in the range of 17%–35.6%. The REI of the collector is calculated based on Eq. (14) as follows:

$$REI = \left(\frac{Eff_{120 \text{ tubes}}}{Eff_{No-tube}} - 1 \right) * 100 \quad (14)$$

4.2. CFD simulation results and discussion

In Fig. 9 and Table 7, the simulation results are validated with experimental data to show the quality of the CFD simulation performed in this study. Three temperature probes in the experimental setup are used to validate the simulation data. As demonstrated in Fig. 9, the temperature CFD simulation values have an acceptable agreement with the experimental data in both cases. Fig. 9 shows the radial temperature variation simulated for the air inside the collector at the parallel surface 0.1 m below the collector. The 120-tube case shows a sharp decrease in temperature adjacent to the collector wall, followed by a sharp increase. In Fig. 9 and Table 7, the simulation findings are validated with experimental data to show the quality of the CFD simulation performed in this study. Three temperature probes in the experimental setup are used to validate simulation data. As demonstrated in Fig. 9, the temperature CFD simulation values have an acceptable agreement with the experimental data in both cases. Fig. 9 shows the radial temperature variation simulated for the air inside the collector at the parallel surface of 0.1 m below the canopy. The 120-tube case shows a sharp decrease in temperature adjacent to the collector wall, followed by a sharp increase. This trend is created because of the inlet airflow. The intense trend in temperature near the wall can be considered due to the effect of the hot wall around the collector. The discontinuous sections represent the hung metallic tubes in the 120-tube chart. It is concluded from the no-tube case that the metallic tubes are performing the role of higher sources of heat arranged inside the collector at different radii. The no-tube case

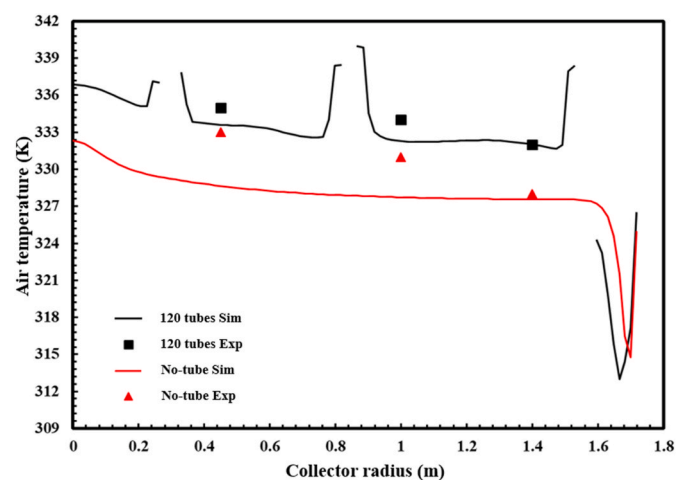


Fig. 9. Profiles of air temperature in the collector versus collector radius for both cases no-tube and 120 tubes; comparison of simulation and experiment results (at 13:00).

represents a uniform temperature increase from the higher to lower radii, appearing just after a sharp decrease in the trend. The air temperature increases after entering the cold air into the collector. Thus, the different warmed-up surfaces of the tubes, which result from efficiently absorbing the reflected radiation inside the tubes, help attain higher airflow temperatures inside the collector compared to the no-tube collector.

Furthermore, Table 7 tabulates exact numerical data compared to experimental data in this study to demonstrate CFD errors. Table 7 shows a maximum error of 1.2% variation between experimentally and numerically achieved values, reflecting as a satisfactory agreement between experimental and numerical results.

4.2.1. Distribution of temperature and velocity

Fig. 10 shows a top view of isothermal contours and streamlines distributions in the collector at a height equal to 0.1 m below the canopy surface but parallel to it. A gradual increase in temperature and velocity is expected to appear in the Fig. 10 (a) from the high radii toward the low radii. However, contrary to this expectation, these contours have no recognizable variation in temperature or velocity. This characteristic appears since the radial temperature variations are not severe in the measurements done inside the collector. This conclusion is well comparable to that provided in Fig. 6 from experimental measurements. However, based on Fig. 10 (b), it can be seen that the spaces near the tubes are hotter than those between the tubes, especially in the sections of upstream airflow relative to the metallic tube surfaces.

Fig. 11 gives a 2D vertical cross-section of the air temperature profile inside the collector and chimney. In Fig. 11 (b), the cold ambient air at the entrance locations to the collector, where the airflow faced the first-row tubes, then changed direction toward the bottom of the collector in the 120-tube case. On the other hand, the cold ambient air at the entrance in the no-tube case is illustrated in Fig. 11 (a), which faces the big circulation loop; as a result, it is directed to the bottom of the collector. The extensive circulation loop acts as an obstacle, forcing the inlet airflow to the center of the collector, where it goes to the chimney. In the 120-tube case, the air inlet goes toward the tubes, creating a smaller circulation loop than in the no-tube case. Furthermore, maximum air temperature happens at the center of the collector in the no-tube case, while it can be seen that temperature is well distributed in the 120-tube case. In addition, the maximum air temperature in the 120-tube case is higher than the no-tube case, about 7 K, which shows that tubes give more energy to the setup.

Due to a better perspective on the airflow field, Fig. 12 shows velocity contours and streamlines in different sections of the solar chimney by no-tube and 120-tubes. The maximum air velocity happens at the chimney entrance in both cases (Fig. 12 (a, b)). To be more specific, in the no-tube case (Fig. 12 (c)), the air velocity is well distributed, whereas in the 120-tube case (Fig. 12 (d)), it is channelized between tubes, and in both cases, the maximum air velocity concentrates at the center of the chimney in the radius cross-section. The maximum air velocity in the 120-tube case is about 8% higher than in the no-tube case, confirming that the presence of the hung metallic tubes increases the air velocity in the collector. The cold air entering the collector is absorbed by hanging metallic tubes that act as heat absorbers. Then, due to the effect of buoyancy, the heated air exiting the chimney goes up. Air movement depends on shear stress, which is the primary cause of the large vortex. As can be seen, although a large loop of air circulation is created in the no-tube case (Fig. 12 (e)), this circulation loop becomes smaller in the 120-tube case (Fig. 12 (f)). However, metallic tubes act as a barrier that changes the airflow direction compared to the no-tube case, where the airflow goes straight along the predicted routes. This action goes toward better mixing of hot and cold air because the large loop breaks into smaller loops. As shown in Fig. 12 (e) and (f), due to the vast difference in airflow velocity between the collector and the chimney entrance, the range of the legend needs to be reduced to see the contours that indicate the direction of the airflow velocity under the collector.

Table 7
Validation for CFD simulation results against experimental data.

Thermometer number	Temperature	No tube			120 tubes		
		Experimental (K)	CFD (K)	Difference (%)	Experimental (K)	CFD (K)	Difference (%)
1	T(R ₁)	333	328.88	1.2	335	333.69	0.3
2	T(R ₂)	331	327.72	0.9	334	332.27	0.5
3	T(R ₃)	328	327.58	0.1	332	331.3	0.2

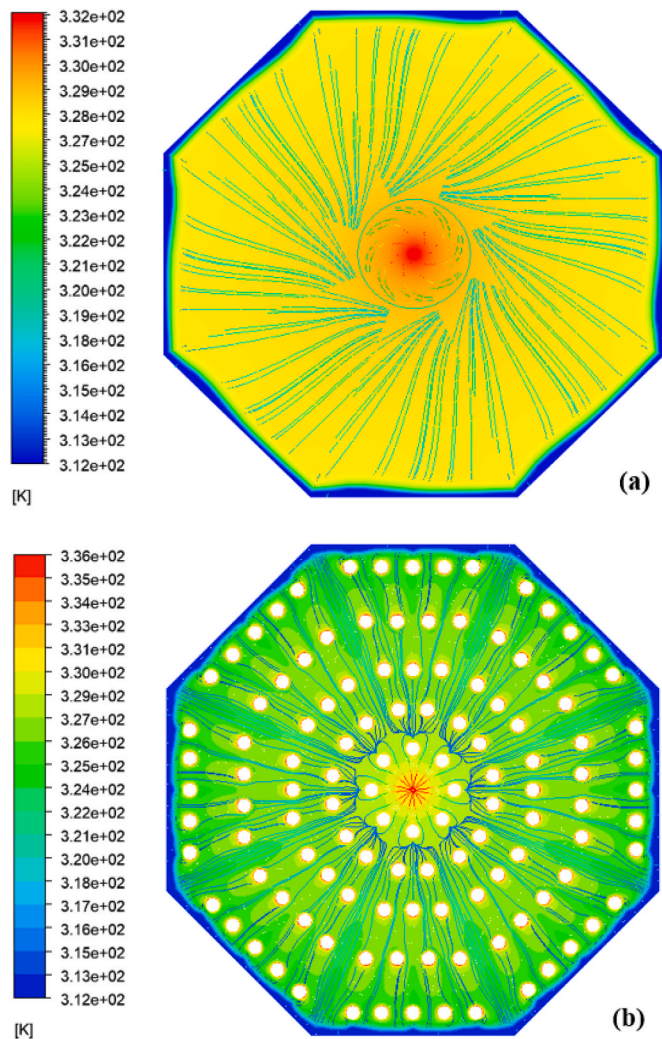


Fig. 10. Airflow temperature distribution contour inside the collector, a) no-tube, b) 120-tube (at 13:00).

Fig. 13 represents the different air velocity profiles (simulation data) from the bottom of the solar chimney to the end of chimney height (at the central axis of the solar chimney) from 12:00 to 14:00. It is obvious that maximum and minimum air velocities occur in 120-tube and no-tube cases at 13:00, about 3.44 and 2.89 m/s, respectively. The highest air velocity occurs a little above the inlet chimney, about 0.8 m in the height of the solar chimney, and then air velocity decreases by about 14%, approximately in all cases. This sharp air velocity increases because of a decrease in the chimney's inlet surface area and a sudden pressure drop. Then, after a gradual decrease, the air velocity becomes stable with some fluctuation.

4.2.2. The effect of different tube geometries on collector efficiency

According to the current research findings, the solar chimney with metallic tubes suspended from the collector's canopy is more efficient

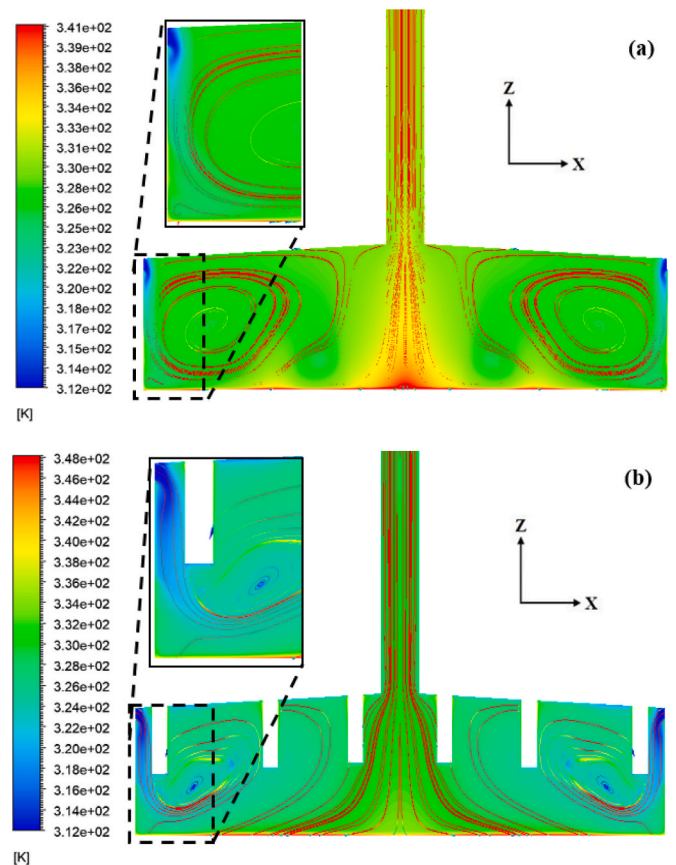
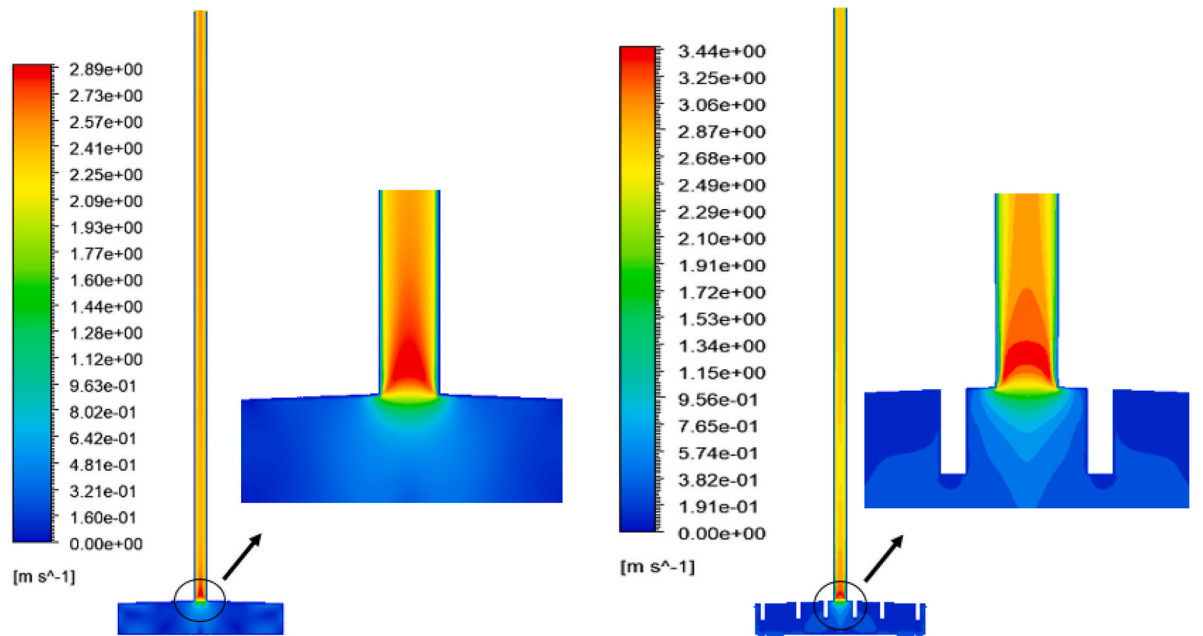


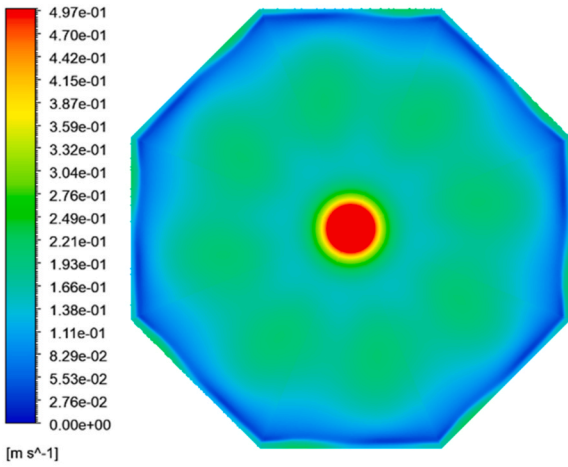
Fig. 11. The contour of the airflow temperature profile of the collector and chimney at the vertical cross-section, a) no-tube, b) 120-tube (at 13:00).

than the no-tube system in all circumstances. Therefore, the effect of metallic tube geometries on the collector's efficiency is studied and compared, as shown in Table 8. By increasing the tube geometry, such as tube height (Lt) and diameter (Dt), the pressure drop, mass flow rate, and velocity are increased. As Lt and Dt grow, the amount of solar energy absorbed by the tubes improves due to the increased effective contact surface between the metallic tube and the air under the collector, enhancing heat transfer between them. Therefore, the absorbed heat results in higher temperatures, and the considerable changes in air density increase natural convection, consequently increasing the airflow velocity in the collector and chimney inlet. To begin, changing tube diameter significantly impacts pressure drop, mass flow rate, and velocity. Where these numbers are higher than those achieved with tube geometry changes, the highest efficiency occurs at (Lt/Dt = 1.83) when changing tube diameter (about 33.7%). Secondly, increasing tube diameter is more effective than increasing tube length because of the increased surface area of the tube, but it causes an increased pressure drop. Finally, although increasing the diameter of the tube has limitations, high efficiency is more attainable in this structure since it causes increasing velocity in the chimney, which brings more airflow rate to the system.

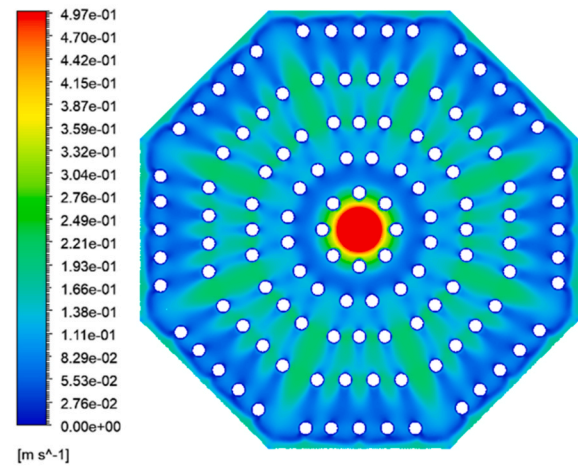


a) Distribution of internal airflow velocity in the collector no-tube (at 13:00).

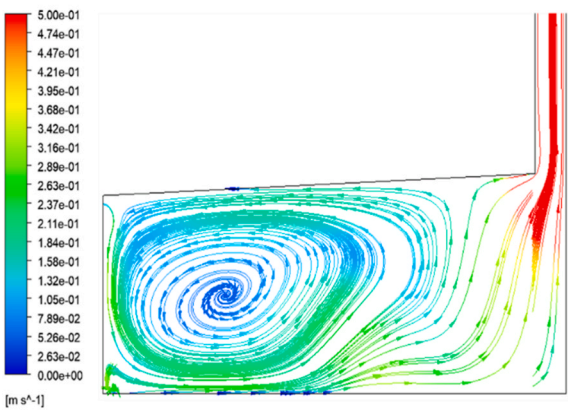
b) Distribution of internal airflow velocity in collector 120-tubes (at 13:00).



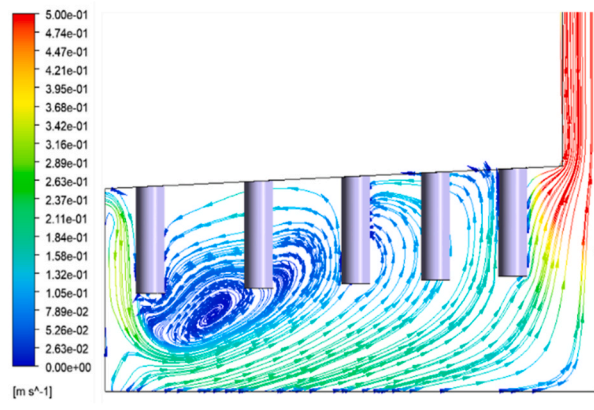
c) Air velocity contour at 0.58 m beneath the collector surface in the no-tube (at 13:00).



d) Air velocity contour at 0.58 m beneath the collector surface in the 120 tubes (at 13:00).



e) Streamlines of velocity in the case of no-tube (at 13:00).



f) Velocity streamlines of the case 120 tubes (at 13:00).

Fig. 12. Contours and streamlines of the solar chimney in different cross-sections (at 13:00).

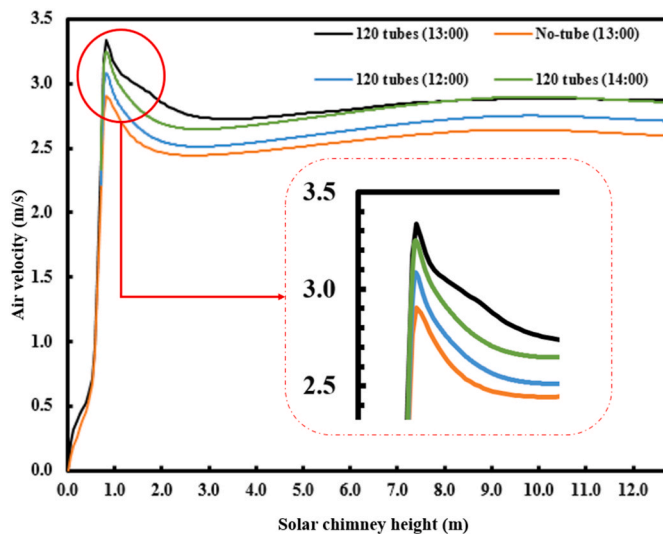


Fig. 13. Simulation results of the airflow velocity distribution versus solar chimney height.

Contours of different geometrical parameters are given in Figs. S8 and S9; Appendix.

4.3. Research comparison

Fig. 14 compares the data of some different collectors provided in the literature with our results. There are many effective geometrical and operational parameters as well as specific novelties that impact the performance of the collector. These are summarized in Table 9 for the cases presented in Fig. 14, which gives the variation of the exiting temperature from the collector against day-time for various studies given in the literature, including our two cases discussed in this research. It would emphasize that the chimney height in our study is the same as that of (No.4) in Table 9. In Fig. 14, higher performance of the SCPP with 120 tube compared to other experimental SCPPs can be achieved until mid-afternoon. The opposite trend is also true for SCPP after noon, with decreasing solar radiation and ambient temperature. Moreover, the performances (temperature) are widely different, which means our technique (hung metallic tubes from the canopy of the collector) is more efficient and has a superior operating condition in evaluating other solar chimneys in Table 9.

5. Conclusions and future research

The collector's efficiency is one of the critical issues in developing SCCP technology. It severely affects the land area required for a specific power production project. In this research, it has been shown that hanging the heat transmission tubes from the canopy of the collector impacts the performance of the solar chimney by increasing surface area

Table 8

The effect of different tube geometries on collector efficiency.

	L_t/D_t	Mass flow (kg/s)	Pressure drop (Pa)	Temperature gradient (K)	Velocity average (m/s)	Collector efficiency (%)
No tube	–	0.0160	2.9346	14.1092	2.245305	25.1153
With 120 tubes	0.23	0.0176	3.4912	16.2108	2.3888	27.0632
$D_t = 0.1$ m (constant)	0.33	0.0181	3.6914	17.1343	2.4565	28.9350
$H_{chim} = 12$ m	0.43	0.0185	3.8103	17.3615	2.4955	28.9078
	0.53	0.0185	3.8636	17.5332	2.5135	30.6691
With 120 tubes	6.6	0.0180	3.6360	16.4141	2.4395	28.1609
$L_t = 0.33$ m (constant)	3.3	0.0181	3.6914	17.1343	2.4565	28.9350
$H_{chim} = 12$ m	2.2	0.0183	3.7900	17.5082	2.4890	29.6356
	1.83	0.0190	4.0906	18.8493	2.5862	33.7179

and reducing radiation heat loss to the deep layers of the ground. The 120 metallic tubes were tested and simulated to reveal the effects of using metallic tubes in the collector's canopy of solar chimneys. The results of the investigations can be briefly stated as follows:

1. The maximum air temperature difference between the collector's inlet and outlet was up to 16.5 K and 22 K for no-tube and 120-tube cases, respectively, which occurred at 13:00.
2. The highest collector heat-absorbing efficiency (in the experimental work) was exactly 25% for the no-tube collector, and this efficiency was increased by about 34% for hung metallic tubes (at 13:00).
3. With 120 metallic tubes hanging from the canopy of the collector, it was achieved that the air temperature at the outlet of the collector increased from 0.5 to 5 K during the day-time measurements from 10:00 to 19:00, compared to the no-tube case, where the airflow velocities in the 120-tube case were about 0.2 m/s higher than the no-tube case in each hour.
4. The maximum REI was 35.6%, which appeared at 13:00 in the testing time range of 11:00 to 15:00 because of the intensified radiation heat.
5. The hung metallic tubes from the canopy of the collector work as the straight heat transfer medium instead of the soil on the ground. Thus, the heat lost to the depths of the land does not happen, resulting in an additional enhancement in air temperature.
6. In terms of changes in metallic tube geometries (diameter and length), the most significant collector efficiency was achieved at over 33.7% by changing the tube diameter, while changing the tube length increased the collector efficiency by just over 30%.

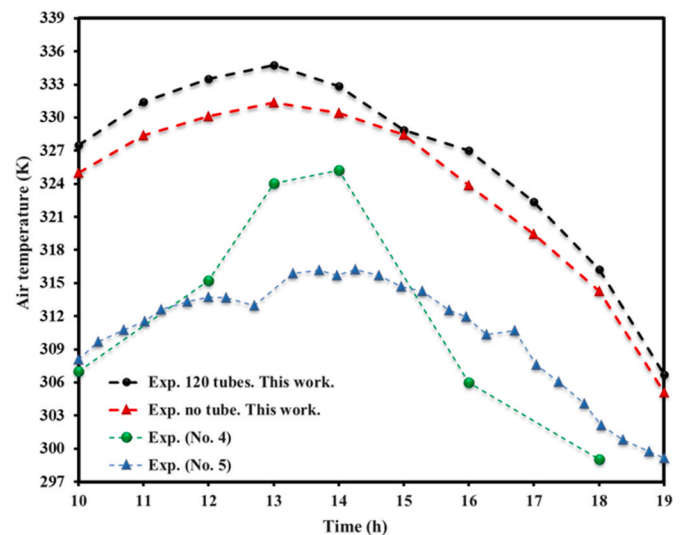


Fig. 14. The experimental airflow temperatures at the collector exit versus time for a sample day. (Exp. No. refer to Table 9).

Table 9

Research comparison related to the specifications of the collectors of some solar chimneys.

No.	Region	Ambient temperature (K)	Collector radius (m)	Chimney height (m)	Chimney diameter (m)	Objective	Research outline	Ref.
1	Tehran	312	1.72	12	0.25	Hung metallic tubes from the canopy of the collector	The maximum air velocity of 2.4 m/s results in the maximum collector efficiency of 33.9%	This work
2	Tehran	313	1.72	12	0.25	No tube	The maximum air velocity of 2.2 m/s results in he maximum collector efficiency to 25.1%	This work
3	Xi'an Jiaotong Simulation of Spain plant (No. 5)	–	–	–	–	Soil heat storage	The large outflow of heated fluid from the chimney outlet becomes the main cause for the energy loss of the system, and canopy also causes considerable energy loss.	Guo et al. (2016)
4	Zanjan	303.5	5	12	0.25	Investigation of climatic effects	The maximum air velocity of 3 m/s.	Kasaieian et al. (2011)
5	Manzanares	–	122	194.6	10.16	Preliminary test results pilot plant	The efficiency of the collector 32%	Haaf (1984)

Finally, according to the promising results obtained in current research and literature, sole solar chimneys have several limitations, such as low efficacy, a large land requirement, dependence on weather conditions, a high construction cost, limited scalability, challenges with thermal management, and a lack of practical studies. These limitations can be circumvented by implementing various strategies, like using advanced materials to enhance the performance of the collector; increasing the height of the chimney; adding concentrators to the collector like mirrors or lenses; using a heat exchanger to preheat the air entering the collector or extract heat from the air leaving the chimney; using multiple chimneys; implementing advanced control systems; and hybridizing with other renewable energy sources. These are all scenarios to increase the efficiency of the solar chimney and make it more competitive with other renewable energy technologies that can be considered for future work.

CRediT authorship contribution statement

Loghman Rezaei: Methodology, Software, Validation, Investigation; **Samrand Saeidi:** Conceptualization, Investigation, Formal analysis, Data curation, Writing – original draft; **András Sápi:** Project administration, Formal analysis, Resources, Writing – review & editing; **MR Abdollahi Senoukesh:** Resources, Investigation, Writing – review & editing; **Gyula Gróf:** Resources, Writing – review & editing; **Wei-Hsin Chen:** Data curation, Writing – review & editing; **Zoltán Kónya:** Supervision, Writing – review & editing; **Jiří Jaromír Klemes:** Investigation, Writing – review & editing.

Declaration of competing interest

The authors declare that they have no known competing financial interests or personal relationships that could have appeared to influence the work reported in this paper.

Data availability

No data was used for the research described in the article.

Acknowledgements

AS gratefully acknowledges the support of the Bolyai Janos Research Fellowship of the Hungarian Academy of Science and the “ÚNKP-22-5-SZTE-587” New National Excellence Program as well as the funding provided by the Indo-Hungarian TÉT project (2019-2.1.13-TÉT_IN-2020-00015) and FK 143583 of NKFIH and Project no. TKP2021-NVA-19 under the TKP2021-NVA funding scheme of the Ministry for

Innovation and Technology and ZK is grateful for K_21 138714 and SNN_135918 project from the source of the National Research, Development and Innovation Fund. The Ministry of Human Capacities through the EFOP-3.6.1-16-2016-00014 project and the 20391-3/2018/FEKUSTRAT are acknowledged. Project no. RRF-2.3.1-21-2022-00009, titled National Laboratory for Renewable Energy has been implemented with the support provided by the Recovery and Resilience Facility of the European Union within the framework of Programme Széchenyi Plan Plus.

Appendix A. Supplementary data

Supplementary data to this article can be found online at <https://doi.org/10.1016/j.jclepro.2023.137692>.

References

- Al-Dabbas, M., 2012. The first pilot demonstration: solar updraft tower power plant in Jordan. *Int. J. Sustain. Energy* 31 (6), 399–410.
- Al-Kayiem, H.H., Aja, O.C., 2016. Historic and recent progress in solar chimney power plant enhancing technologies. *Renew. Sustain. Energy Rev.* 58, 1269–1292.
- Al-Kayiem, H.H., Yin, K.Y., Sing, C.Y., 2012. Numerical Simulation of Solar Chimney Integrated with Exhaust of Thermal Power Plant. WIT Press, United Kingdom.
- Amudam, Y., Chandramohan, V., 2019. Influence of thermal energy storage system on flow and performance parameters of solar updraft tower power plant: a three dimensional numerical analysis. *J. Clean. Prod.* 207, 136–152.
- Ansys Inc, F., 2013. Users Guide.
- Arzpeyma, M., Mekhilef, S., Newaz, K.M., Horan, B., Seyedmahmoudian, M., Akram, N., Stojceviski, A., Alnaimat, F., Mathew, B., 2022. Numerical simulation of the effect of chimney configuration on the performance of a solar chimney power plant. *J. Therm. Anal. Calorim.* 147 (3), 2549–2563.
- Asnaghi, A., Ladjevardi, S.M., 2012. Solar chimney power plant performance in Iran. *Renew. Sustain. Energy Rev.* 16 (5), 3383–3390.
- Ayadi, A., Bouabidi, A., Driss, Z., Abid, M.S., 2018. Experimental and numerical analysis of the collector roof height effect on the solar chimney performance. *Renew. Energy* 115, 649–662.
- Ayadi, A., Driss, Z., Bouabidi, A., Abid, M.S., 2017. Experimental and numerical study of the impact of the collector roof inclination on the performance of a solar chimney power plant. *Energy Build.* 139 (15), 263–276.
- Campos, D., 2016. Handbook on Navier-Stokes Equations: Theory and Applied Analysis. Nova Science Publisher, s, Incorporated.
- Cao, F., Li, H., Ma, Q., Zhao, L., 2014. Design and simulation of a geothermal–solar combined chimney power plant. *Energy Convers. Manag.* 84, 186–195.
- Cao, F., Zhao, L., Guo, L., 2011. Simulation of a sloped solar chimney power plant in Lanzhou. *Energy Convers. Manag.* 52 (6), 2360–2366.
- Dai, Y.J., Huang, H.B., Wang, R.Z., 2003. Case study of solar chimney power plants in Northwestern regions of China. *Renew. Energy* 28 (8), 1295–1304.
- Esen, H., Ozgen, F., Esen, M., Sengur, A., 2009a. Artificial neural network and wavelet neural network approaches for modelling of a solar air heater. *Expert Syst. Appl.* 36 (8), 11240–11248.
- Esen, H., Ozgen, F., Esen, M., Sengur, A., 2009b. Modelling of a new solar air heater through least-squares support vector machines. *Expert Syst. Appl.* 36 (7), 10673–10682.
- Fadaei, N., Kasaieian, A., Akbarzadeh, A., Hashemabadi, S.H., 2018. Experimental investigation of solar chimney with phase change material (PCM). *Renew. Energy* 123, 26–35.

- Fallah, S.H., Valipour, M.S., 2022. Numerical investigation of a small scale sloped solar chimney power plant. *Renew. Energy* 183, 1–11.
- Fasel, H.F., Meng, F., Shams, E., Gross, A., 2013. CFD analysis for solar chimney power plants. *Sol. Energy* 98, 12–22.
- Fathi, N., McDaniel, P., Aleyasin, S.S., Robinson, M., Vorobieff, P., Rodriguez, S., de Oliveira, C., 2018. Efficiency enhancement of solar chimney power plant by use of waste heat from nuclear power plant. *J. Clean. Prod.* 180, 407–416.
- Ghalamchi, M., Kasaieian, A., Ghalamchi, M., 2015. Experimental study of geometrical and climate effects on the performance of a small solar chimney. *Renew. Sustain. Energy Rev.* 43, 425–431.
- Ghalamchi, M., Kasaieian, A., Ghalamchi, M., Mirzahassemi, A.H., 2016. An experimental study on the thermal performance of a solar chimney with different dimensional parameters. *Renew. Energy* 91, 477–483.
- Gholamalizadeh, E., Kim, M.-H., 2014. Three-dimensional CFD analysis for simulating the greenhouse effect in solar chimney power plants using a two-band radiation model. *Renew. Energy* 63, 498–506.
- Guo, P.-h., Li, J.-y., Wang, Y., 2014. Numerical simulations of solar chimney power plant with radiation model. *Renew. Energy* 62, 24–30.
- Guo, P., Li, J., Wang, Y., Wang, Y., 2015. Numerical study on the performance of a solar chimney power plant. *Energy Convers. Manag.* 105, 197–205.
- Guo, P., Li, T., Xu, B., Xu, X., Li, J., 2019. Questions and current understanding about solar chimney power plant: a review. *Energy Convers. Manag.* 182, 21–33.
- Guo, P., Wang, Y., Li, J., Wang, Y., 2016. Thermodynamic analysis of a solar chimney power plant system with soil heat storage. *Appl. Therm. Eng.* 100, 1076–1084.
- Haaf, W., 1984. Solar chimneys: part ii: preliminary test results from the Manzanares pilot plant. *J. Int. J. Sust. Energy* 2 (2), 141–161.
- Hu, S., Leung, D.Y., Chan, J.C., 2017. Impact of the geometry of divergent chimneys on the power output of a solar chimney power plant. *Energy* 120, 1–11.
- Kasaieian, A.B., Heidari, E., Nasiri Vatan, S., 2011. Experimental investigation of climatic effects on the efficiency of a solar chimney pilot power plant. *Renew. Sustain. Energy Rev.* 15 (9), 5202–5206.
- Kebabsa, H., Lounici, M.S., 2021. Performance evaluation of the combined solar chimney-photovoltaic system in Algeria. *J. Clean. Prod.* 321, 128628.
- Koonsrisuk, A., Chitsomboon, T., 2013. Mathematical modeling of solar chimney power plants. *Energy* 51, 314–322.
- Krzywanski, J., Sztokler, K., Szubel, M., Siwek, T., Nowak, W., Mika, L., 2020a. A comprehensive three-dimensional analysis of a large-scale multi-fuel CFB boiler burning coal and syngas. Part 1. The CFD model of a large-scale multi-fuel CFB combustion. *Entropy* 22 (9), 964.
- Krzywanski, J., Sztokler, K., Szubel, M., Siwek, T., Nowak, W., Mika, L., 2020b. A comprehensive, three-dimensional analysis of a large-scale, multi-fuel, CFB boiler burning coal and syngas. Part 2. Numerical simulations of coal and syngas co-combustion. *Entropy* 22 (8), 856.
- Li, J., Guo, H., Cheng, Q., Huang, S., 2017. Optimal turbine pressure drop for solar chimney-aided dry cooling system in coal-fired power plants. *Energy Convers. Manag.* 133, 87–96.
- Mehranfar, S., Ghareghani, A., Azizi, A., Andwari, A.M., Pesyridis, A., Jouhara, H., 2022. Comparative assessment of innovative methods to improve solar chimney power plant efficiency. *Sustain. Energy Technol. Assessments* 49, 101807.
- Ming, T., Liu, W., Pan, Y., Xu, G., 2008. Numerical analysis of flow and heat transfer characteristics in solar chimney power plants with energy storage layer. *Energy Convers. Manag.* 49 (10), 2872–2879.
- Ming, T., Wu, Y., K.de Richter, R., Liu, W., Sherif, S.A., 2017. Solar updraft power plant system: a brief review and a case study on a new system with radial partition walls in its collector. *Renew. Sustain. Energy Rev.* 69, 472–487.
- Muhammed, H.A., Atrooshi, S.A., 2019. Modeling solar chimney for geometry optimization. *Renew. Energy* 138, 212–223.
- Najafi, A., Jafarian, A., Darand, J., 2019. Thermo-economic evaluation of a hybrid solar-conventional energy supply in a zero liquid discharge wastewater treatment plant. *Energy Convers. Manag.* 188, 276–295.
- Nasraoui, H., Driss, Z., Kchaou, H., 2020. Novel collector design for enhancing the performance of solar chimney power plant. *Renew. Energy* 145, 1658–1671.
- Nizetic, S., Ninic, N., Klarin, B., 2008. Analysis and feasibility of implementing solar chimney power plants in the Mediterranean region. *Energy* 33 (11), 1680–1690.
- Ozgen, F., Esen, M., Esen, H., 2009. Experimental investigation of thermal performance of a double-flow solar air heater having aluminium cans. *Renew. Energy* 34 (11), 2391–2398.
- Patel, S.K., Prasad, D., Ahmed, M.R., 2014. Computational studies on the effect of geometric parameters on the performance of a solar chimney power plant. *Energy Convers. Manag.* 77, 424–431.
- Pretorius, J.P., 2007. Optimization and Control of a Large-Scale Solar Chimney Power Plant. University of Stellenbosch, Stellenbosch.
- Rabehi, R., Chaker, A., Ming, T., Gong, T., 2018. Numerical simulation of solar chimney power plant adopting the fan model. *Renew. Energy* 126, 1093–1101.
- Sabziparvar, A.A., Shetaee, H., 2007. Estimation of global solar radiation in arid and semi-arid climates of East and West Iran. *Energy* 32 (5), 649–655.
- Saha, S., Ruslan, A.R.M., Monjur Morshed, A., Hasanuzzaman, M., 2021. Global prospects and challenges of latent heat thermal energy storage: a review. *Clean Technol. Environ. Policy* 23 (2), 531–559.
- Sajjadi, M., Shirvani, M., Yousefi, M.R., Afsari, H., Rezaei, L., Ghanadi, M., 2021. Day and night times performance improvement of the solar chimney by combining with the CSP system. *Appl. Sol. Energy* 57 (4), 310–322.
- Schlaich, J., Bergemann, R., Schiel, W., Weinrebe, G., 2004. Sustainable electricity generation with solar updraft towers. *Struct. Eng. Int.* 14 (3), 225–229.
- Sharon, H., 2023. A Detailed Review on Sole and Hybrid Solar Chimney Based Sustainable Ventilation, Power Generation, and Potable Water Production Systems. *Energy Nexus*, 100184.
- Xu, G., Ming, T., Pan, Y., Meng, F., Zhou, C., 2011. Numerical analysis on the performance of solar chimney power plant system. *Energy Convers. Manag.* 52 (2), 876–883.
- Yapıcı, E.Ö., Ayli, E., Nsaif, O., 2020. Numerical investigation on the performance of a small scale solar chimney power plant for different geometrical parameters. *J. Clean. Prod.* 276, 122908.
- Zhou, X., Xu, Y., 2016. Solar updraft tower power generation. *Sol. Energy* 128, 95–125.
- Zou, Z., He, S., 2015. Modeling and characteristics analysis of hybrid cooling-tower-solar-chimney system. *Energy Convers. Manag.* 95, 59–68.